Customizable Acoustic Metamaterial Barrier with Intelligent Sound Insulation

Zihao Su,[‡] Hao Luo,[‡] Siyuan Gao, Zhitao Luo, Yifan Zhu,[*] and Hui Zhang[†]
Jiangsu Key Laboratory for Design and Manufacture of Micro-Nano Biomedical Instruments, School of Mechanical Engineering, Southeast University, Nanjing 211189, China

(Received 19 July 2022; revised 7 October 2022; accepted 16 November 2022; published 12 December 2022)

Conventional acoustic metamaterial barriers are usually used to realize sound insulation for a continuous broad bandwidth. In some practical scenes, however, the noise signal from complex noise sources, such as gearboxes and motors, are usually complicated spectra with discrete peaks or valleys, instead of perfect continuous ones. In this case, the broadband design is unnecessary and may increase the thickness of metamaterials if too many frequency components are included. We need only a customized spectrum to achieve sound insulation at desired discrete frequencies, while, at other ones, insulation can be unwanted to preserve an effective signal other than noise. Here, we propose a customizable acoustic metamaterial barrier (CAMB) with intelligent and selective sound insulation. The CAMB is a composite structure consisting of a Helmholtz resonator (HR) and a microperforated panel (MPP) destined to control sound insulation at low frequencies, within 200–1000 Hz, and high-frequencies, within 1000–3000 Hz, respectively. An inverse process is proposed for customizable design. We use analytical and numerical methods to obtain the design libraries for the parameters of the HRs and MPPs. We numerically and experimentally demonstrate an example of a CAMB customized for a practical complex noise source. The sample has a thickness of 48 mm, approximately λ/11 for the lowest targeted frequency. The proposed customizable concept may pave the way for acoustic insulating metamaterials for complex sound sources with different frequency components.

DOI: 10.1103/PhysRevApplied.18.064029

I. INTRODUCTION

Sound insulation [1,2] and sound absorption [3] are two approaches for noise control and are also significant and fundamental topics in acoustics. Conventional natural sound-absorbing materials, such as sound-absorbing sponges, have reduced performance in the low-frequency range. In comparison, acoustic metamaterials [4,5] and metasurfaces [6] have improved performances, including high efficiency and small thickness. Previous works have used multiple resonant unit cells, such as Helmholtz resonators [7,8], Fabry-Perot tubes [9–12], and membranes [13–17], or nonlocal coupling effects [18] to obtain a broad bandwidth, the width of which is usually larger than one octave. Additionally, they have also proposed ventilation and sound-insulation structures [19,20] to deliberately realize ventilation and sound-insulation simultaneously [21–25].

In practical scenes, however, different noise sources may result in a complex noise-frequency spectrum. For example, the noise from a motor or gearbox usually has specific eigenfrequencies, which are determined by the engagement of gears [26–28], leading to very high or low components for single or discrete frequencies. Therefore, the noise-frequency spectrum of a practical device is always determinate instead of random. In this case, the broadband design is unnecessary and may increase the thickness of a metamaterial if too many frequency components are included. Different resonant frequency units in broadband acoustic metamaterial designs may occupy extra space, increasing the structural complexity and processing cost.

To solve these issues, we conceive an alternative strategy by proposing the concept of a customizable acoustic metamaterial barrier (CAMB) with intelligent and selective sound insulation. A CAMB is a composite structure consisting of a Helmholtz resonator (HR) [29] and a microperforated panel (MPP) [30], corresponding to controllable sound insulation for low frequency, within 200–1000 Hz, and high frequency, within 1000–3000 Hz, respectively. An inverse process is used for customizable design. We employ analytical and numerical methods to achieve the design libraries for the parameters of the HRs and MPPs. Different from a conventional single HR, we study the coupling effects between multiple resonators and their relevant geometric parameter dependences, which may affect their acoustic impedances. We numerically and experimentally demonstrate an example of a CAMB that is

---

[*] yifanzhu@seu.edu.cn
[†] seuzhanghui@seu.edu.cn
[‡] Z. Su and H. Luo contributed equally to this work.

customized for a complex industrial-noise source. The fabricated sample has a thickness of 48 mm, approximately $\lambda/11$ for the lowest targeted frequency. The proposed customizable concept could pave the way to acoustic metamaterial insulation for different sound sources with complex frequency components.

II. THEORY AND METHOD

A. Concept of a customizable acoustic metamaterial barrier

A general design route for a CAMB is shown in Fig. 1(a). We first analyze the frequency spectrum for a target noise source and characterize it with multiple featured frequency points. Featured frequency points include a featured low-frequency peak (FLFP) and a featured high-frequency valley (FHFV). Then, based on both the FLFP and FHFV, we decide on the parameter selections for the CAMB from design libraries. A CAMB can be designed for various types of noise source with different frequency characteristics, and the final target is to achieve intelligent sound insulation with low transmission and a planar frequency spectrum for transmitted waves.

Figures 1(b)–1(d) illustrate the structural schematic diagram of a CAMB. The incident wave propagates into the CAMB, consisting of HRs and a MPP. For low-frequency manipulation, HRs are used as resonant unit cells to achieve sound insulation at the targeted frequency to manage FLFPs. For high-frequency sound insulation, the MPP is a good candidate to manage the FHFV. The detailed three-dimensional (3D) structure of the CAMB is shown in Figs. 1(c) and 1(d). In the structural schematic diagram, we show only the case of one HR with a light disk-shaped geometry.

As shown in Figs. 1(c) and 1(d), the CAMB consists of a MPP, back cavity, and HR, where the back cavity is defined as the space between the MPP and HR [6]. Here, the MPP with the back cavity is the high-frequency working area, while the HR is a low-frequency working area, as marked by the dashed boxes. It is worth mentioning that the number of HRs is not fixed (1, 2, 3...) and determined by the low-frequency characteristics of the incident noise. For a better understanding of the acoustic performance of each part, the equivalent circuit model of the CAMB is displayed in Fig. 1(c). The MPP and the neck of the HR exhibit acoustic resistance and acoustic mass characteristics, respectively. The cavities of the HR exhibit acoustic capacitance characteristics. We also consider the coupling effect from the open region between the back cavity and HRs, which can be extra acoustic mass.

The sectional view of the CAMB is shown in Fig. 1(d). More details and the geometric properties of the CAMB in Fig. 1(c) can be described by the diameter, d_{MPP}, of the holes of the MPP; the thickness, t, of the MPP; the side length, H; the perforation rate, $\sigma = d_{\mathrm{MPP}}^2(n-1)^2/4H^2$ (n is the number of perforations on a single side); and D is the depth of the back cavity. The light disk-shaped HR's geometric parameters are given in the figure and the inset. R is the radius of the HR, d is the diameter of the open region, r_{neck} is the radius of the neck, W is the width of the HR cavity, and W_{neck} is the width of the neck. The HR's cavity-wall thickness is 1 mm. R_e in Fig. 1(d) is the effective radius, an important parameter for calculating the HR's acoustic impedance, which is discussed later.

The sound-transmission loss (L_{ST}) is defined as $L_{\mathrm{ST}} = -10\log_{10}(T)$, where T is the transmission coefficient of sound intensity. In our model, the L_{ST} is calculated by

$$L_{\mathrm{ST}} = -10\log_{10}\left[\left(\frac{2Z_0\sigma}{2Z_0\sigma + Z_{\mathrm{MPP}}}\right) \times \left(\frac{|Z_{\mathrm{HR}}|^2}{\left(\frac{Z_0}{2S_b} + \mathrm{Re}(Z_{\mathrm{HR}})\right)^2 + \mathrm{Im}(Z_{\mathrm{HR}})^2}\right)\right], \qquad (1)$$

where $Z_0 = \rho_0 c_0$ is the acoustic impedance of air, $\rho_0 = 1.21\ \mathrm{kg/m^3}$ is the mass density of air, and $c_0 = 343$ m/s is the sound speed in air. $S_b = \pi d^2/4$ is the area of the open region. Z_{MPP} is the acoustic impedance of the MPP, and Z_{HR} is the acoustic impedance of the HR.

The small hole on the MPP can be regarded as a narrow tube with a small diameter relative to the distance between holes. The impedance of the MPP can be calculated as [30]

$$Z_{\mathrm{MPP}} = j\omega\rho_0 t\left[1 - \frac{2}{K\sqrt{-j}}\frac{J_1\left(K\sqrt{-j}\right)}{J_0\left(K\sqrt{-j}\right)}\right]^{-1}, \qquad (2)$$

where ω is the angular frequency, t is the thickness of the MPP, $\mu = 1.983 \times 10^{-5}$ Pa is the dynamic viscosity of air, J_n is the nth order of the Bessel function of the first kind, the $K = d_{\mathrm{MPP}}\sqrt{\omega\rho_0/\mu}/2$. The diameter of the holes affects the impedance of the MPP and thermal dissipation.

During the interaction of incident waves with the HR, the whole HR resonator can be treated as a spring-mass oscillator system [29]. R_n is the acoustic resistance induced by the effects of radiation and thermal viscosity and is calculated by [31]

$$R_n \approx \frac{8l}{\pi w_n^3}\sqrt{2\mu\omega\rho_0} + 8\frac{\sqrt{2\mu\omega\rho_0}}{\pi w_n^2} + \frac{4\rho_0 c_0}{\pi w_n^2} \times \left[1 - \frac{2J_1(kw_n)}{kw_n}\right], \qquad (3)$$

where w_n is the equivalent radius and $k = \omega/c_0$ is the wave number.

The acoustic capacitance and acoustic mass can jointly determine the sound-insulation frequency of the HR. The acoustic capacitance of the HR is $C_{\mathrm{HR}} = V_0/\rho_0 c_0^2$ and the

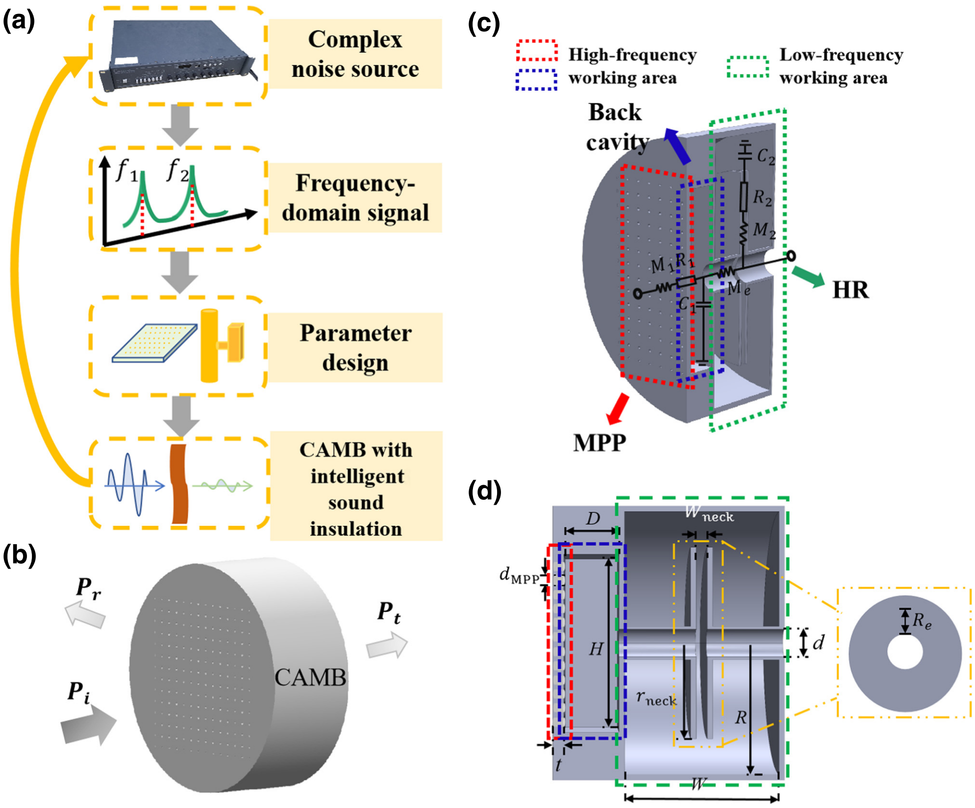

FIG. 1. Concept of a CAMB. (a) General design route of a CAMB. (b) Schematic diagram of the CAMB. Arrows indicate incident, reflected, and transmitted waves. (c) 3D structure and effective circuit model of the CAMB. It consists of MPP, back cavity, and HR. Case with one HR is shown here. (d) Sectional view of the CAMB in (c) with $t = 1$ mm, $H = 65$ mm, $D = 10$ mm, $R = 48$ mm, $d = 10$ mm, $r_{\text{neck}} = 35$ mm, $W_{\text{neck}} = 2$ mm, $W = 28$ mm, and $d_{\text{MPP}} = 1$ mm. In the inset, R_e is the effective radius. Dashed boxes (red, blue, and green) indicate operating frequency bands of the different parts in (c),(d).

acoustic mass is $M_{\text{HR}} = \rho_0 L/S$; V_0 is the volume of the HR cavity, $L = r_{\text{neck}} - d/2$ is the length of the neck, and S is the effective cross-section area of the neck. Different from a conventional HR, the cross-section area in the radial direction of the neck in this work is gradient varying. To get the relationship between the neck's effective cross-section area, S, and other geometric parameters, we define an effective radius, R_e, to estimate S, namely, $S = 2\pi(R_e + d/2)W_{\text{neck}}$, as indicated in the inset of Fig. 1(d).

Then, the effective impedance of the HR is calculated by $Z_{\text{HR}} = j(\omega M_{\text{HR}} - 1/\omega C_{\text{HR}}) + R_n$, and the resonant frequency of the HR (corresponding to the FLFP) is calculated as

$$j(\omega M_{\text{HR}} - 1/\omega C_{\text{HR}}) = 0. \tag{4}$$

In the design, we change the length of the neck, L, to obtain the R_e value. Figure 2(a) shows the simulated results of the CAMB. The peak frequencies of L_{ST} represent the resonant frequencies of the HR for different L. Substituting into Eq. (4), we can get different neck effective cross-section areas, S, to calculate R_e. Simulated values (red circles) and fitted curve (blue line) for the effective radius, R_e, changing with L are shown in Fig. 2(b). The fitted curve is expressed as

$$R_e = 0.2909L - 0.526L^2. \tag{5}$$

Furthermore, the HR's volume parameters, W, H_e, and the separation of the neck (W_{neck}), are investigated to analyze the effects of the geometric parameters on R_e. We define H_e as $H_e = R - d/2$. By changing W and H_e, the volume of the HR cavity and resonant frequency also change. It can be seen from Fig. 2(c) that the resonant frequencies vary from 300 to 416 Hz. Interestingly, R_e is approximately stable and very close to the value at $L = 30$ mm. A similar conclusion can also be drawn from Figs. 2(e) and 2(f). R_e values in Fig. 2(f) are slightly different from the calculated R_e. Therefore, R_e is only affected by L, and we can design HRs in the CAMB by changing the parameter R_e.

B. Numerical simulation and experimental demonstration

To study the relationship between structural parameters and the sound-insulation frequency, the CAMB is numerically simulated by using the "Pressure Acoustics Module" and the "Thermoviscous Acoustics Module" in COMSOL Multiphysics and results are also verified experimentally.

Figure 3(a) illustrates the analytical values based on Eq. (4) and simulated results for the FLFP, in the low-frequency range from 300 to 1000 Hz. Then, we conduct research on low-frequency sound insulation at multiple frequency points for the targeted FLFPs. The low-frequency working area is divided into two independent parts (two

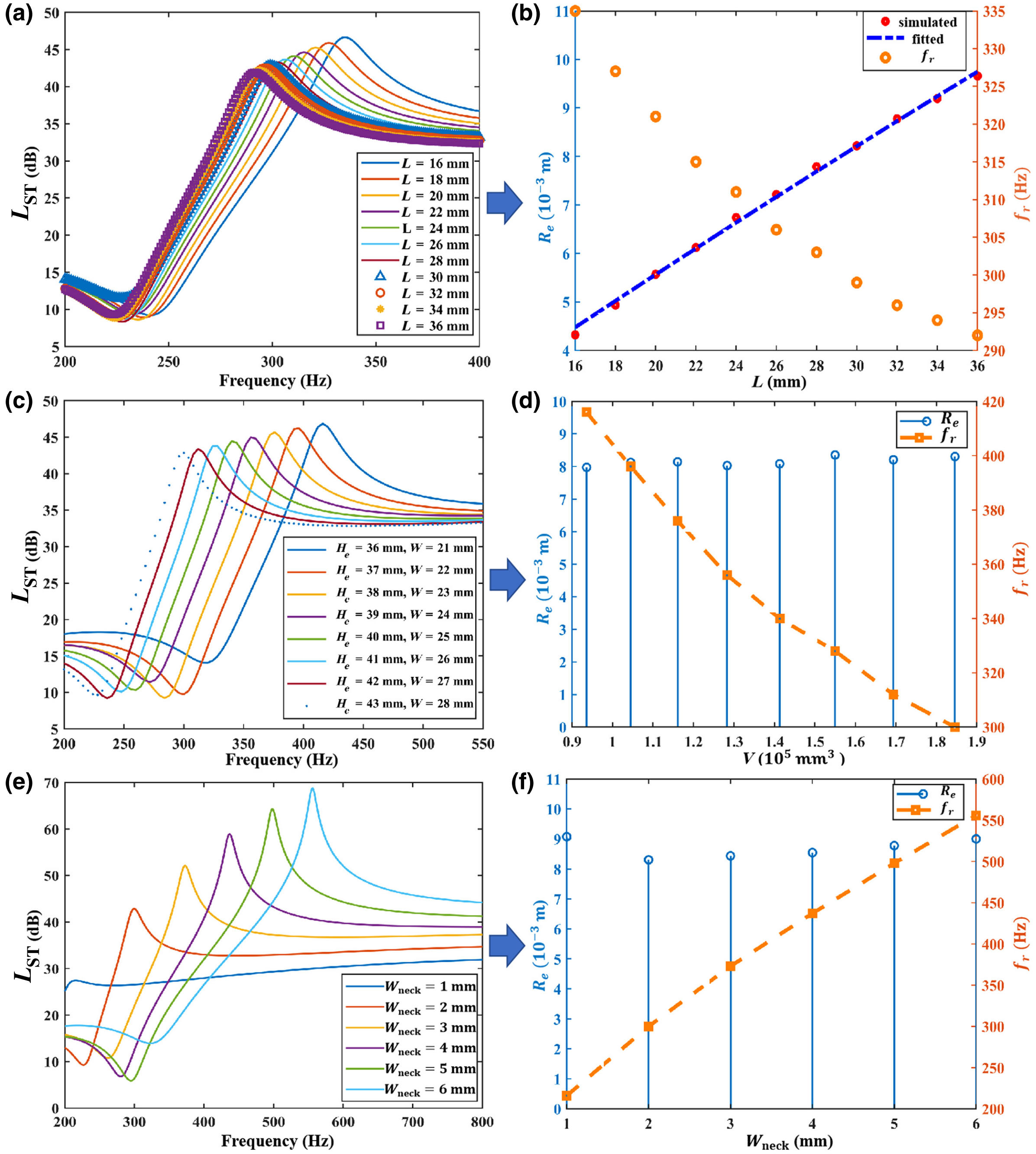

FIG. 2. Design library of a single HR. (a) Simulation of L_{ST} for L. (b) Relationship between L; resonant frequency, f_r; and effective radius, R_e. $L = r_{neck} - d/2$. Other parameters are the same as in Fig. 1(d). (c) Simulation of L_{ST} for different volume parameters. $H_e = R - d/2$. (d) Effective radius, R_e, and resonant frequency, f_r, for different volumes. V represents the volume of HR, which is calculated based on W and H_e. (e) Simulation of L_{ST} for W_{neck}. (f) Effective radius, R_e, and resonant frequency, f_r, for W_{neck}.

flabellate HRs), and the circular sector angle, θ, as marked in Fig. 3(b) should be lower than 180°. By changing the geometric parameters, R_e, the resonant frequency of each HR, is adjusted. Since the circumferential coverage angles of the HR's neck and cavity are the same, they can be eliminated in the process of calculating the expression of resonant frequency. The calculation method is the same as that for a single cavity.

For parallel cavities, we assume the impedance of the cavities as Z_1 and Z_2, so the wave equation can be

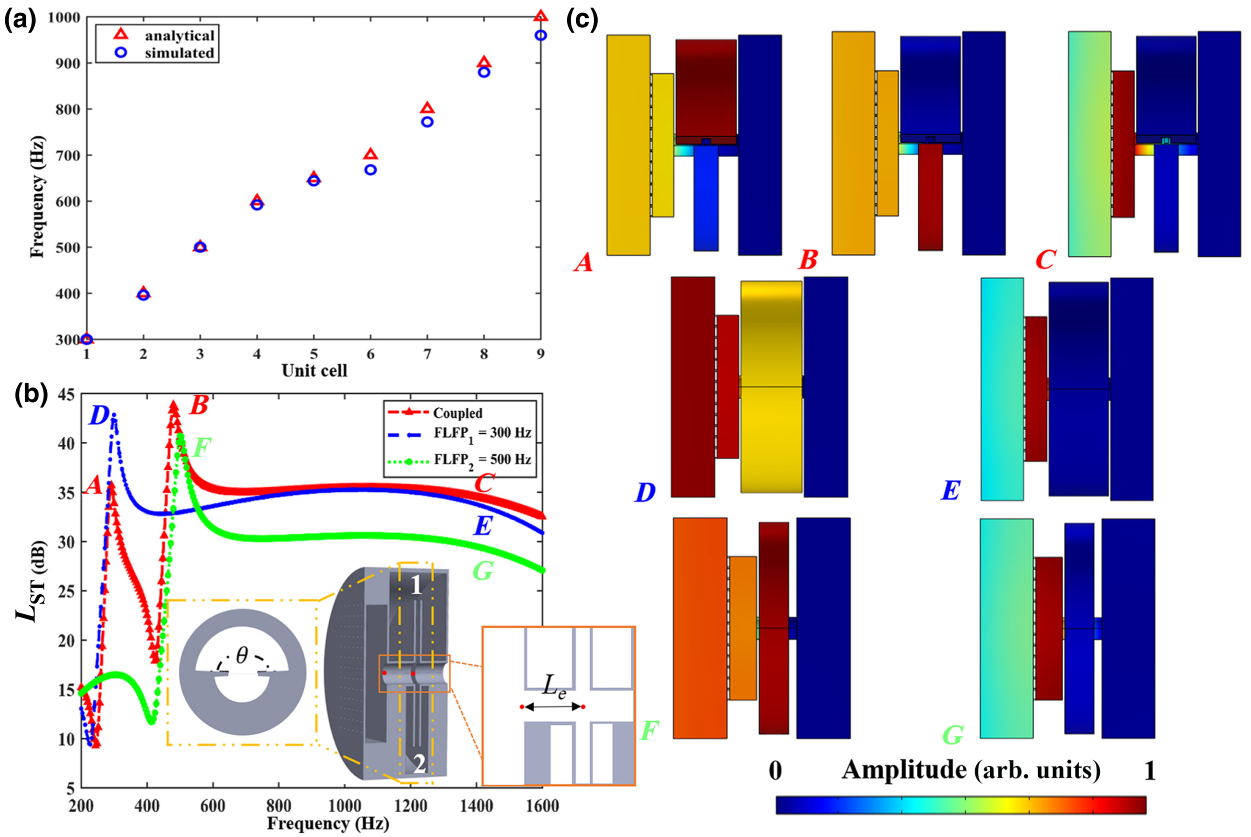

FIG. 3. Design of coupled HRs for low-frequency modulations. (a) Difference between analytical values calculated from Eq. (4) and simulated ones. (b) Simulation of L_{ST} for different FLFPs. Inset is a schematic of the basic unit with two HRs. Circumferential coverage angle, θ, is 175°. Geometric parameters of HR 1 are the same as those in Fig. 1(d), and W of HR 2 is 11.3 mm. A, 292 Hz, coupled; B, 480 Hz, coupled; C, 1400 Hz, coupled; D, 300 Hz, $\mathrm{FLFP}_1 = 300$ Hz; E, 1400 Hz, $\mathrm{FLFP}_1 = 300$ Hz; F, 500 Hz, $\mathrm{FLFP}_2 = 500$ Hz; G, 1400 Hz, $\mathrm{FLFP}_2 = 500$ Hz. L_e is the length of the open region between the MPP and HRs. (c) Acoustic-pressure-field distributions correspond to the points in (b).

expressed as

$$\frac{\partial^2 p(x,\omega)}{\partial x^2} + \left[\left(\frac{\omega}{c_0}\right)^2 + j\left(\frac{Z_0}{Z_1} + \frac{Z_0}{Z_2}\right)\frac{\omega}{c_0}\delta(x - x_0)\right] p(x,\omega) = 0, \tag{6}$$

where $\delta(x)$ is the Dirac function, and x_0 is the position of the HR resonator. Equation (6) reveals the nature of low-frequency sound isolation. Each HR acts as a local resonance unit coupling with radiation waves. The results presented in Fig. 3(b) demonstrate the frequency shift and Fano-like interference induced by the coupling resonance [32]. The inset illustrates the inner structure of the metamaterial barrier, and the circumferential coverage angle, θ, is 175°. The geometric parameters of HR 1 are the same as those in Fig. 1(d), and the parameters of HR 2 are changed for 500 Hz based on Eqs. (4) and (5) by adjusting only W. The structure possesses an asymmetric L_{ST} valley, as shown in Fig. 3(b), due to destructive interference based on Fano-like interference. The coupling of two local resonance units forms an antiresonance point, which achieves low-frequency discrete sound insulation.

The acoustic-pressure-field distributions are shown in Fig. 3(c), and the red color indicates the working parts at these frequencies. The HR plays an important role in low-frequency insulation for a targeted FLFP. In the coupled case, HR 1 and HR 2 work for two different frequencies (FLFPs). The sound-pressure-field distributions marked by A–G correspond to points A–G in Fig. 3(b). A and B demonstrate that HR 1 and HR 2 resonate at 292 and 480 Hz, respectively, for the coupled structure with targeted $\mathrm{FLFP}_1 = 300$ Hz and targeted $\mathrm{FLFP}_2 = 500$ Hz. With only one cavity, the simulated acoustic-pressure-field distribution exhibits a very similar resonant state, as shown in D and F. The validity of the analytical derivations is demonstrated for both single and multiple HR cases.

The high-frequency characteristics of the MPP (including the back cavity) offer a stable high-frequency sound-insulation bandwidth with L_{ST} higher than 20 dB, for both cases of a single HR (D–G) and multiple HRs (A–C).

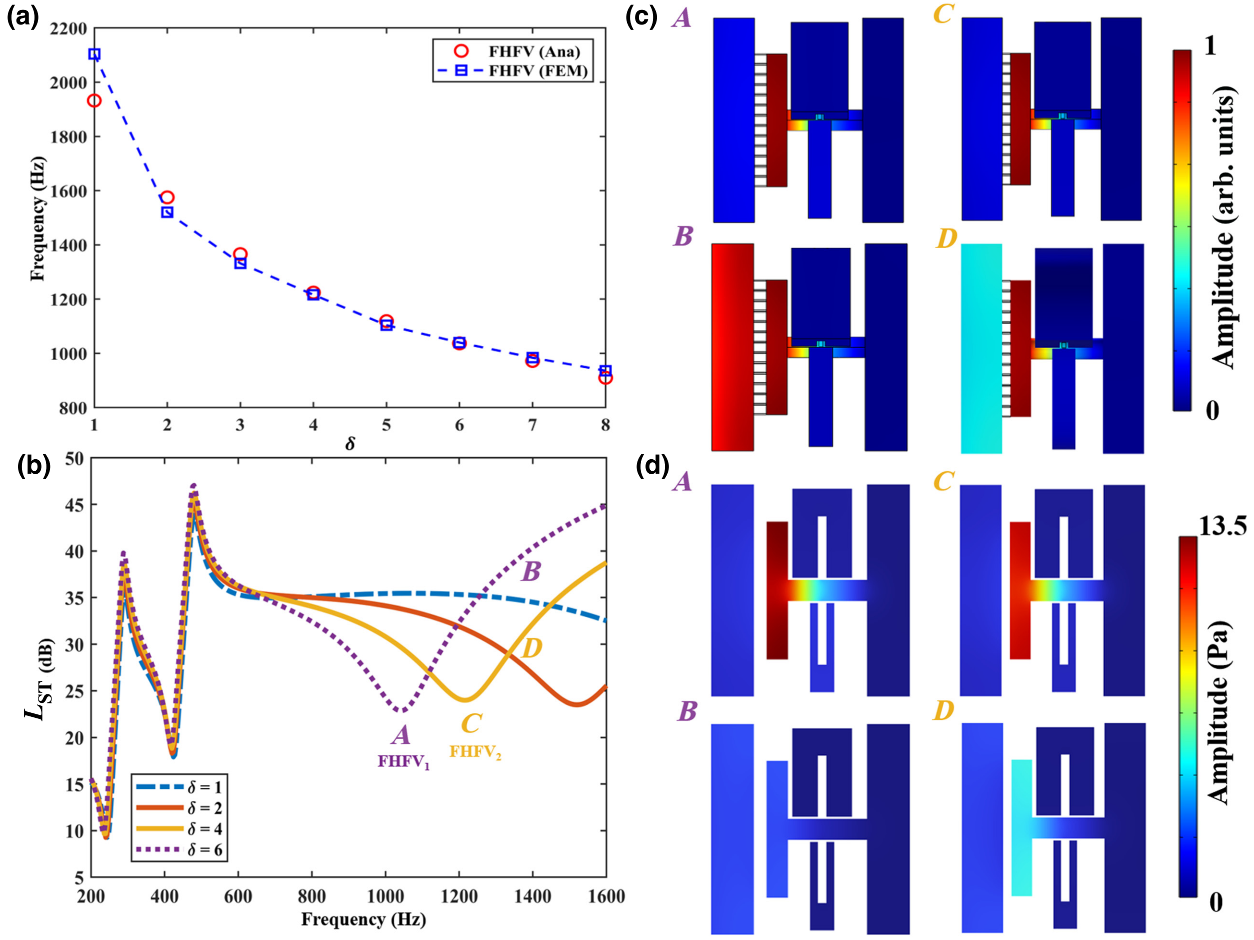

FIG. 4. Design library of the MPP and design of coupled composite structure for high-frequency modulations. (a) Analytical [calculated with Eq. (7)] and FEM results of the FHFV for different δ of the MPP. (b) Simulation of L_{ST} of the FHFV for different δ. (c) Simulated acoustic pressure field; *A*, FHFV$_1$= 1040 Hz, $\delta = 6$; *B*, 1400 Hz, $\delta = 6$; *C*, FHFV$_2$ = 1216 Hz, $\delta = 4$; *D*, 1400 Hz, $\delta = 4$. (d) Axial-plane sectional view. Color illustrates the acoustic-pressure-field distribution corresponding to modes *A*–*D* in (b).

The thickness of the MPP is changed to modulate the high-frequency behavior of metamaterial barriers. In the general MPP, t and d_{MPP} are important parameters that determine the resonance frequency. Herein, we define a parameter, $\delta = t/d_{\mathrm{MPP}}$, to discuss the influence of t and d_{MPP} on the FHFV. d_{MPP} is the same as before and t is changed from 1 to 8 mm. Due to the existence of the coupling effect, the open region between the MPP and HRs can be regarded as extra acoustic mass, M_e. Herein, $M_e = \rho_0 L_e/S_b$, where L_e is the length of the open region between the MPP and HRs, shown in the inset of Fig. 3(b); S_b is the same as in Eq. (1). Considering the structures attached behind the MPP, we introduce a correction factor, $\zeta \propto M_e$, to represent extra relative acoustic mass to calculate the FHFV. For convenience, we use the relative acoustic impedance by dividing with the term $\rho_0 c_0$ from Eq. (2). Then, the FHFV is determined by [30]

$$\omega m + \zeta - \cot(\omega D/c_0) = 0, \tag{7}$$

where $m = M/\rho_0 c_0$ is the relative acoustic mass, ωm is the relative acoustic mass reactance of MPP, and $\cot(\omega D/c_0)$ is the relative acoustic reactance of the back cavity. The FHFV of the CAMB is obtained by numerical analysis and the finite-element method (FEM), respectively. The results are shown in Fig. 4(a). The FHFV decreases with the thickness of the MPP when D is 10 mm, and the agreement between analytical results and the finite-element method proves the effectiveness of the model, providing a theoretical foundation to manipulate the FHFV.

Figure 4(b) shows the simulation results for different MPP thicknesses. The MPP has little effect on the FLFP at low frequencies, which ensures the decoupled modulation between FHFV and FLFP of the CAMB. To further analyze the valley effect, we display the acoustic-pressure-field distribution for $\delta = 4$ and 6 at the FHFV and 1400 Hz in Fig. 4(c). Different from the performance at low frequency, at high frequency, due to the existence of the MPP, back cavity, and extra acoustic mass, it exhibits two

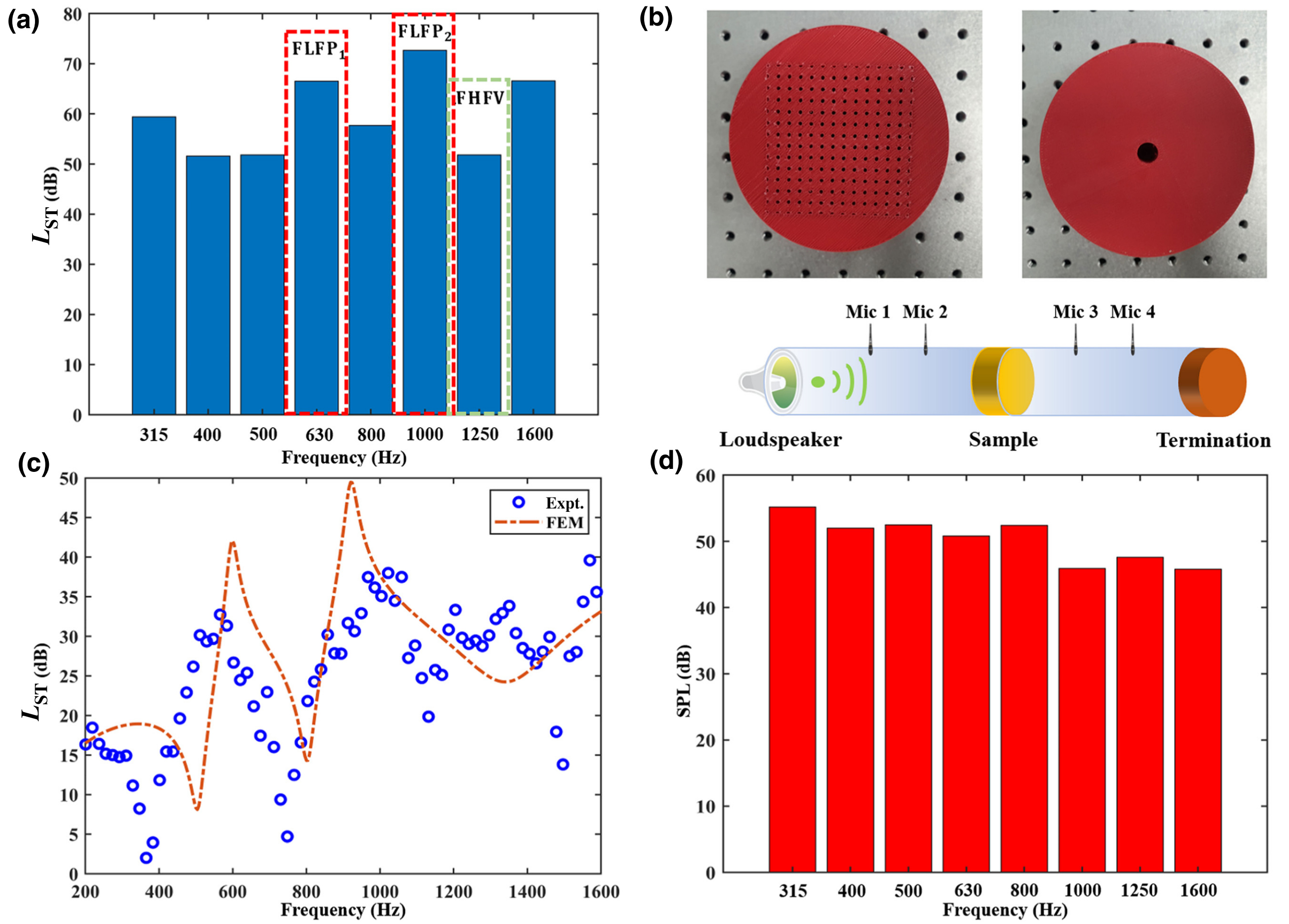

FIG. 5. Experimental realization of a CAMB. (a) Analysis of a specific complex noise source. Spectrogram is measured by a sound-level meter with a resolution of 1/3 octave. FLFP and FHFV are read from the spectrogram, as marked in the figure. $\text{FLFP}_1 = 630$ Hz, $\text{FLFP}_2 = 1000$ Hz, and $\text{FHFV} = 1250$ Hz. (b) Photograph of the 3D printed sample. Sample front (left) and back (right) views and the experimental setup. (c) Simulated and experimental L_{ST} within 200–1600 Hz. (d) Noise spectrum after sound insulation by the CAMB.

modes of reflection and radiation. Figure 4(d) shows the axial-plane sectional view, and the red color implies high acoustic pressure. At modes A and C, the highest acoustic pressure close to 13.5 Pa (incidence is set as 1 Pa) appears in the back cavity and penetrates through almost the entire open region, displaying the radiation property. In modes B and D, the pressure at the back cavity is at a low level, and the pressure of the background-pressure field is greater than A and C. This means that, at high frequencies, when the MPP is not in resonance, the structure exhibits reflective properties. Based on the valley effect, we can control the FHFV at high frequencies.

In the following study, we show the experimental realization of the CAMB for a specific noise source, in which the HR, MPP, and all geometry parameters jointly guarantee selectivity and the sound-insulation performance. We first measure the noise spectrum of specific equipment, as shown in Fig. 5(a). The signal-collection equipment is a Type-BSWA308 sound-level meter. From the 1/3 octave curve, one reads the FLFPs and FHFV as $\text{FLFP}_1 = 630$ Hz, $\text{FLFP}_2 = 1000$ Hz, and $\text{FHFV} = 1250$ Hz, as marked in Fig. 5(a).

Then, the sample is designed and fabricated for targeted $\text{FLFP}_1 = 630$ Hz and targeted $\text{FLFP}_2 = 1000$ Hz at low frequency and targeted $\text{FHFV} = 1250$ Hz at high frequency. We get the following structural parameters from the design libraries. For MPP, $d_{\text{MPP}} = 2$ mm, $t = 11$ mm, $H = 65$ mm, $D = 15$ mm. In this case, δ is 5.5, and based on Eq. (7), $\text{FHFV} = 1250$ Hz. For the HR, the geometric parameters at $\text{FLFP} = 630$ Hz are $R_1 = 34$ mm, $r_{\text{neck1}} = 21$ mm, $W_{\text{neck1}} = 2$ mm, and $W_1 = 17.4$ mm. At $\text{FLFP} = 1000$ Hz, $R_2 = 30$ mm, $r_{\text{neck2}} = 15$ mm, $W_{\text{neck2}} = 2$ mm, and $W_2 = 11.7$ mm. $d = 10$ mm. L_e is 10 mm, and the total thickness of the CAMB is only 48 mm, approximately $\lambda/11$.

Figure 5(b) shows the experimental sample made of acrylonitrile butadiene styrene via 3D printing. The sample is measured in a lab-made impedance tube, as schematically shown in Fig. 5(b). The four-microphones method [6] is adopted to measure the transmission loss of the CAMB. Figure 5(c) shows a comparison of L_{ST} obtained by simulation and experiment. In the FEM, the simulated $\mathrm{FLFP}_1 = 600$ Hz, $\mathrm{FLFP}_2 = 924$ Hz; moreover, FHFV appears at 1340 Hz. The small errors between the simulated featured frequencies and the target ones are due to slight coupling in the composite structure. The experimental results are in good agreement with the simulation, indicating the effectiveness of this CAMB sample. A fine selectivity and sound insulation can be observed, which demonstrates the fine performance of the CAMB. The difference between simulation and experiment is mainly induced by the error of sample fabrication.

Finally, to verify the actual selective sound-insulation performance, we also measure the noise-frequency spectrum after sound insulation by the CAMB. We put the sound-level meter and the sound source at the two ends of the impedance tube for measurement. The noise signal measured in Fig. 5(d) is relatively flat, which proves that the CAMB has fine customizability for the noise signal in Fig. 5(a), making the final signal balanced. The averaged sound pressure level (L_{SP}) for the noise source in Fig. 5(a) is 59.8 dB, and the averaged L_{SP} after noise insulation by the CAMB in Fig. 5(d) is 50.3 dB. Thus, the averaged noise insulation is 9.5 dB.

III. CONCLUSION

We conceptually conceive and design a CAMB based on composite structures comprised of a MPP and a HR. The proposed model is adapted by introducing the effective radius, R_e, and a correction factor, ζ. For binary HRs, the coupling effect between different parts that offer discrete insulation points is studied. The MPP provides more convenience for high-frequency noise control. Simulation results demonstrate the tunability of the FLFP and FHFV, and the bandwidth study in the Appendix A demonstrates that FHFV manipulations can be raised to 3000 Hz. It is worth mentioning that, compared with previous works, the diverse parameters of the CAMB offer several degrees of freedom to optimize device performance and tunability. By suitably designing the geometry of the units, sound waves can be controlled with proper frequency components. The sample is designed with featured frequencies at 630, 1000, and 1250 Hz. Simulated and experimental results demonstrate the fine selectivity and sound insulation within 200–1600 Hz of the designed structure with a thickness of 48 mm (approximately $\lambda/11$ for the lowest targeted frequency). Additionally, the controllable and intelligent sound-insulation performance of the designed metamaterial is further proved by collecting a specific noise source and comparing the results before and after using the CAMB. Our proposed CAMB may enlighten the field of intelligent metamaterials and lead to noise-control applications in different scenarios, such as industrial manufacturing, vehicles, and architectural acoustics.

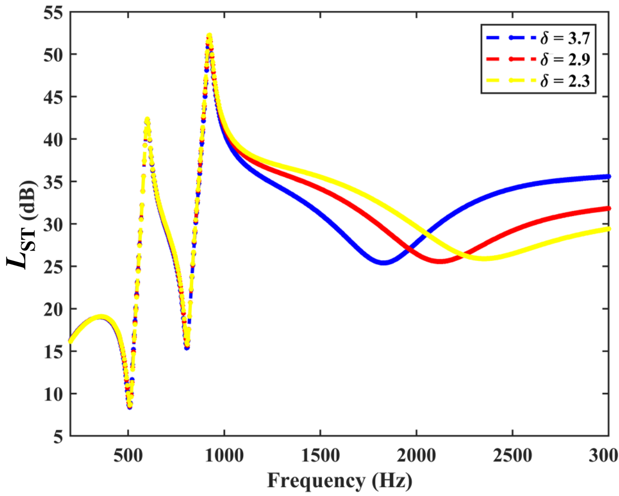

FIG. 6. Simulated results of targeted FHFV at 1800 Hz (blue line), 2100 Hz (red line), and 2400 Hz (yellow line) by changing δ.

ACKNOWLEDGMENTS

This work is financially supported by the National Natural Science Foundation of China (Grants No. 11874110 and No. 52272433), the Natural Science Foundation of Jiangsu Province (Grant No. BK20220798), the Young Elite Scientists Sponsorship Program by JSAST (Grant No. TJ-2022-012), and the Fundamental Research Funds for the Central Universities.

APPENDIX A: BANDWIDTH STUDY

To further investigate the influence of the geometric parameters on the bandwidth of the sound-insulation spectrum, we adjust δ of the sample in Fig. 5(b) to control the FHFV without changing other parameters. The simulated results are shown in Fig. 6. The results show that the high-frequency design library for the MPP is raised to 3000 Hz. According to the variation trend of the FHFV, it is obvious that we can enlarge the frequency range with a wider bandwidth and unchanged thickness by fixing the R_e and W values and changing only the δ value. It also proves the design flexibility of the CAMB.

[1] M. Sun, X. Fang, D. Mao, X. Wang, and Y. Li, Broadband Acoustic Ventilation Barriers, Phys. Rev. Appl. **13**, 044028 (2020).

[2] R. Ghaffarivardavagh, J. Nikolajczyk, S. Anderson, and X. Zhang, Ultra-open acoustic metamaterial silencer based on Fano-like interference, Phys. Rev. B **99**, 024302 (2019).

[3] M. Y. Duan, C. L. Yu, F. X. Xin, and T. J. Lu, Tunable underwater acoustic metamaterials via quasi-Helmholtz resonance: From low-frequency to ultra-broadband, Appl. Phys. Lett. **118**, 071904 (2021).

[4] M. Yang and P. Sheng, Sound absorption structures: From porous media to acoustic metamaterials, Annu. Rev. Mater. Res. **47**, 83 (2017).

[5] S. A. Cummer, J. Christensen, and A. Alu, Controlling sound with acoustic metamaterials, Nat. Rev. Mater. **1**, 16001 (2016).

[6] B. Assouar, B. Liang, Y. Wu, Y. Li, J. C. Cheng, and Y. Jing, Acoustic metasurfaces, Nat. Rev. Mater. **3**, 460 (2018).

[7] L. Shen, Y. F. Zhu, F. L. Mao, S. Y. Gao, Z. H. Su, Z. T. Luo, H. Zhang, and B. Assouar, Broadband Low-Frequency Acoustic Metamuffler, Phys. Rev. Appl. **16**, 064057 (2021).

[8] M. Y. Duan, C. L. Yu, Z. M. Xu, F. X. Xin, and T. J. Lu, Acoustic impedance regulation of Helmholtz resonators for perfect sound absorption via roughened embedded necks, Appl. Phys. Lett. **117**, 151904 (2020).

[9] Y. F. Zhu, S. W. Fan, L. Y. Cao, K. Donda, and B. Assouar, Acoustic Meta-Equalizer, Phys. Rev. Appl. **14**, 014038 (2020).

[10] M. Yang, S. Y. Chen, C. X. Fuab, and P. Sheng, Optimal sound-absorbing structures, Mater. Horizons **4**, 673 (2017).

[11] C. R. Liu, J. H. Wu, Z. R. Yang, and F. Y. Ma, Ultra-broadband acoustic absorption of a thin microperforated panel metamaterial with multi-order resonance, Compos. Struct. **246**, 112366 (2020).

[12] Y. F. Zhu, K. Donda, S. W. Fan, L. Y. Cao, and B. Assouar, Broadband ultra-thin acoustic metasurface absorber with coiled structure, Appl. Phys. Express **12**, 114002 (2019).

[13] Z. Yang, H. M. Dai, N. H. Chan, G. C. Ma, and P. Sheng, Acoustic metamaterial panels for sound attenuation in the 50–1000 Hz regime, Appl. Phys. Lett. **96**, 041906 (2010).

[14] J. Mei, G. C. Ma, M. Yang, Z. Y. Yang, W. J. Wen, and P. Sheng, Dark acoustic metamaterials as super absorbers for low-frequency sound, Nat. Commun. **3**, 756 (2012).

[15] X. L. Wang, H. Zhao, X. D. Luo, and Z. Y. Huang, Membrane-constrained acoustic metamaterials for low frequency sound insulation, Appl. Phys. Lett. **108**, 041905 (2016).

[16] F. Y. Ma, M. Huang, and J. H. Wu, Ultrathin lightweight plate-type acoustic metamaterials with positive lumped coupling resonant, J. Appl. Phys. **121**, 015102 (2017).

[17] F. Langfeldt and W. Gleine, Membrane- and plate-type acoustic metamaterials with elastic unit cell edges, J. Sound Vib. **453**, 65 (2019).

[18] Y. F. Zhu, A. Merkel, K. Donda, S. W. Fan, L. Y. Cao, and B. Assouar, Nonlocal acoustic metasurface for ultra-broadband sound absorption, Phys. Rev. B **103**, 064102 (2021).

[19] S. Kumar and H. P. Lee, Labyrinthine acoustic metastructures enabling broadband sound absorption and ventilation, Appl. Phys. Lett. **116**, 134103 (2020).

[20] C. Shen, Y. B. Xie, J. F. Li, S. A. Cummer, and Y. Jing, Acoustic metacages for sound shielding with steady air flow, J. Appl. Phys. **123**, 124501 (2018).

[21] Y. Cheng, C. Zhou, B. G. Yuan, D. J. Wu, Q. Wei, and X. J. Liu, Ultra-sparse metasurface for high reflection of low-frequency sound based on artificial Mie resonances, Nat. Mater. **14**, 1013 (2015).

[22] J. W. Jung, J. E. Kim, and J. W. Lee, Acoustic metamaterial panel for both fluid passage and broadband soundproofing in the audible frequency range, Appl. Phys. Lett. **112**, 041903 (2018).

[23] H. L. Zhang, Y. F. Zhu, B. Liang, J. Yang, J. Yang, and J. C. Cheng, Omnidirectional ventilated acoustic barrier, Appl. Phys. Lett. **111**, 203502 (2017).

[24] Y. Ge, H. X. Sun, S. Q. Yuan, and Y. Lai, Broadband unidirectional and omnidirectional bidirectional acoustic insulation through an open window structure with a metasurface of ultrathin hooklike meta-atoms, Appl. Phys. Lett. **112**, 243502 (2018).

[25] Z. H. Su, Y. F. Zhu, S. Y. Gao, H. Luo, and H. Zhang, High-efficient and broadband acoustic insulation in a ventilated channel with acoustic metamaterials. Front. Mech. Eng. **8**, 857788 (2022).

[26] R. Barron, *Industrial noise control and acoustics*, 1st ed. (CRC Press, Boca Raton, 2019).

[27] L. Faulkner, *Industrial noise control fundamentals and applications*, 2nd ed. (CRC Press, Boca Raton, 1994).

[28] Jiří Tůma, *Vehicle gearbox noise and vibration* (Wiley, Chichester, West Sussex, 2014).

[29] L. Kinsler, *Fundamentals of acoustics* (Wiley, New York, 1982).

[30] D. Y. Maa, Potential of microperforated panel absorber, J. Acoust. Soc. Am. **104**, 2861 (1998).

[31] G. S. Liu, Y. Y. Peng, M. H. Liu, X. Y. Zou, and J. C. Cheng, Broadband acoustic energy harvesting metasurface with coupled Helmholtz resonators, Appl. Phys. Lett. **113**, 153503 (2018).

[32] T. A. Johansson and M. Kleiner, Theory and experiments on the coupling of two Helmholtz resonators, J. Acoust. Soc. Am. **110**, 1315 (2001).